

A Numerical Study of the Modulation of Short Sea Waves by Longer Waves

Guangdong Pan and Joel T. Johnson, *Senior Member, IEEE*

Abstract—The spatial spectrum of short sea waves is locally modulated by the presence of longer waves or currents; in the remote sensing literature, this process is described by the hydrodynamic modulation transfer function (HMTF). Such modulations are important in understanding radar images of sea waves with water wavelengths longer than the radar range resolution. Existing models for the HMTF utilized in remote sensing are based on approximations derived from consideration of conservation of wave action. However, the accuracy of these approximations has been quantified only through comparison with experimental data; in such comparisons, numerous empirical models for terms such as wind forcing and breaking wave dissipation are required, which make direct evaluation of the hydrodynamic effects difficult. A method for providing direct insight into the hydrodynamic modulation of short sea waves by longer waves is described in this paper, through use of numerical nonlinear hydrodynamic codes for sea surface evolution. The codes applied are reviewed, and a Monte Carlo simulation process based on a stochastic spectrum of short waves propagating over a single deterministic long wave is described, including the data analysis techniques developed to extract a numerical HMTF from the simulated surfaces. HMTF values obtained from the simulations are compared with those from a first-order wave action solution and are found to be in reasonable agreement, although differences on the order of 10% are observed. A numerical evaluation of long wave effects on the short wave dispersion relation is also provided.

Index Terms—Hydrodynamics, modulation transfer function.

I. INTRODUCTION

IT IS well known that the amplitudes and wavenumbers of short water waves are modulated when propagating over an underlying long water wave or current [1], [2]. These modulations represent a nonlinear hydrodynamic interaction between sea waves; such interactions, however, are typically not resonant interactions, so that no secular change of the short wave spectrum occurs with time. Thus, these effects are typically ignored in attempts to model and forecast the sea surface spectrum using an energy balance approach.

Modulations of short waves by longer ocean waves do play an important role, however, in radar imaging of the sea surface. In this case, the commonly applied “two-scale” model of sea backscatter states that radar returns with a specific range cell are produced by short waves (or Bragg waves) within the range cell, observed at the local incidence angle of the range cell. When sea waves of wavelengths larger than the radar range cell

are present within a radar image, the resulting changes in the local incidence angle (“tilt modulations”) across the larger sea waves produce variations in the measured radar cross section image, typically allowing the sea waves to be observed. In addition to the tilt modulation effect, variations in the Bragg wave amplitudes along the long waves through hydrodynamic modulations also produce variations in the radar cross section with range. It is generally assumed in sea radar imaging that the tilt modulation effect is well understood, so that the remaining variations are produced by hydrodynamic effects. This process allows empirical studies of the hydrodynamic modulation transfer function (HMTF) (as in [3]) to be performed through analysis of measured radar images. However, the modulations obtained are influenced by numerous geophysical factors at the time and location of the measurements, so that validating any hydrodynamic theories of the HMTF can be difficult.

Existing analytical theories of the HMTF are primarily based on the concept of conservation of wave action [3]–[7]. In these theories, the basic equations state that the wave action of the short waves is conserved except for the presence of a set of source and dissipation terms. The former includes effects such as short wave generation by either wind forcing, nonlinear interactions, or wave breaking, whereas the latter includes viscous damping and other dissipative effects. Empirical models are utilized to describe most of these contributions. Although it is possible to numerically solve the resulting wave action equations through the method of characteristics, an approximation to first order is typically used in the remote sensing literature to determine the HMTF. At this order, long wave effects appear near identical to those from currents, with the current amplitude equal to the horizontal component of the long wave orbital velocity.

Although this first-order HMTF analysis has been applied in numerous remote sensing studies, significant evidence exists in the literature that this model underpredicts the actual modulations observed [3], [8]. Although such underprediction can be corrected by modifying or adding new source and dissipation terms in the wave action equations, it is difficult to separate the accuracy of the hydrodynamic model from the accuracy in description of source and dissipation terms.

To address this issue, a study of the HMTF is described in this paper based on the use of numerical algorithms for sea surface hydrodynamics. The hydrodynamic algorithm applied is based on the pseudospectral method [9], hereinafter denoted as the Watson–West (WW) approach. This algorithm has been applied previously in studies of gravity wave evolution [9]–[12] as well as radar scattering from the sea surface [13], [14]. Although the pseudospectral method is not exact, it has

Manuscript received February 27, 2006; revised May 5, 2006. This work was supported by the National Office of Naval Defense.

The authors are with the Department of Electrical and Computer Engineering and ElectroScience Laboratory, The Ohio State University, Columbus, OH 43210 USA (e-mail: pan.88@osu.edu; johnson.1374@osu.edu).

Digital Object Identifier 10.1109/TGRS.2006.877756

been shown in numerous studies [9], [10], [12] to provide high-fidelity hydrodynamic simulations so long as the order of the algorithm is sufficiently high and so long as steep features are avoided in the surface evolution. The numerical approach involves Monte Carlo simulation of the hydrodynamic evolution of a spectrum of short sea waves in the presence of either one or two deterministic long waves. Because no wind, wave breaking, or viscous dissipation effects are included in the simulation, the results of this simulation allow assessment of the accuracy of the first-order HMTF often used in practice.

In Section II, the WW algorithm is described, along with the simulation procedure utilized. A method for extracting a “numerical HMTF” from the simulated data is presented in Section III, and results obtained are presented in Section IV. A numerical study of the short wave dispersion relation is described in Section V. Section VI provides a review of the analytical first-order HMTF for comparison with the numerical results. Tests show that the numerical HMTF values are in reasonable agreement with those from the analytical theory, although small differences are observed that indicate that improved formulations of the first-order theory may be desirable. Final remarks are provided in Section VII.

II. NUMERICAL HYDRODYNAMIC SIMULATIONS

A. Formulation

The studies of this paper utilize a one-dimensional (1-D) fluid surface of infinite depth and assume that the fluid is incompressible and inviscid; surface tension effects are also neglected. The surface elevation is denoted as $z = \eta(x, t)$ and the surface velocity potential as $\phi(x, t)$, where (x, z) are the horizontal and vertical space coordinates, respectively, and t represents time. The evolution of these two quantities is determined by [9]

$$\phi_t = -g\eta - \frac{1}{2}\phi_x^2 + \frac{1}{2}\phi_z^2 [1 + \eta_x^2] \quad (1)$$

$$\eta_t = -\phi_x\eta_x + \phi_z [1 + \eta_x^2] \quad (2)$$

where the subscript denotes the associated derivative and g is the gravitational acceleration (9.8 m/s^{-2}). We solve (1) and (2) using the pseudospectral method of [9] and retain terms up to fourth order in the slope expansion.

B. Initial Conditions

Initial conditions for the simulations include one or two deterministic “long” wave(s) and a stochastic spectrum of “short waves” to study modulation of the short wave spectrum. The specific initial condition with one long wave is

$$\eta(x, t = 0) = a_1 \sin(k_1 x) + \eta_s(x) \quad (3)$$

$$\phi(x, t = 0) = -a_1 \sqrt{g/k_1} \cos(k_1 x) + \phi_s(x) \quad (4)$$

where the long wave has wavenumber k_1 and amplitude a_1 . It is assumed that the long wave lies in the gravity wave region, and the initial conditions are developed to produce a long wave

traveling in the \hat{x} direction in the linear hydrodynamic limit. Previous work with such initial conditions [9], [12] shows the tendency of the long wave to approach a Stokes’ wave form for moderate $k_1 a_1$ values. The computational domain is set to 2π meters, and the long wave wavenumber is set to $k_1 = 1 \text{ rad/m}$ in the majority of the results to be shown. Note that a scale transformation is possible for surface composed only of gravity waves, so that these simulations also represent hydrodynamic effects for gravity wave surfaces with the length and height dimensions scaled by a constant.

The initial short wave surface η_s is a realization of a Gaussian random process surface with a Pierson–Moskowitz (P–M) spectrum [13], i.e.,

$$S(k_s) = \frac{0.0081}{4} k_s^{-3} \exp\left(-\frac{0.74g^2}{k_s^2 U_{19.5}^4}\right) \quad (5)$$

where $U_{19.5}$ denotes the surface wind speed at height 19.5 m. This spectrum essentially is a k_s^{-3} spectrum for 1-D surfaces, with a low-frequency rolloff controlled by a wind speed parameter $U_{19.5}$. The initial short wave spectrum is truncated to exist between wavenumbers 30 and 170 rad/m only. The lower limit of 30 rad/m ensures that the short waves are indeed “short” compared with the long wave, whereas the upper limit is chosen based on surface sampling requirements. Although the parameter $U_{19.5}$ was set to 3 m/s, the portion of the P–M spectrum influenced by $U_{19.5}$ has wavenumbers much less than 30 rad/m, so that $U_{19.5}$ has virtually no effect. The short wave velocity potential $\phi_s(x)$ was generated again through a linear, \hat{x} , traveling assumption for each spectral component of $\eta_s(x)$. The generated surface was sampled into 1024 points, providing sufficient resolution to resolve the short wave spectrum while retaining fourth-order computations in the WW method.

Because the linear assumption of the initial conditions does not match the nonlinear nature of (1) and (2), we utilize a “ramp-up” procedure [9], [13] to reduce any discontinuities that may be introduced. In this procedure, all nonlinear terms in the evolution (1) and (2) are multiplied by a ramp-up factor

$$W_R(t) = e^{-\left(\frac{t-a}{b}\right)^2} \quad (6)$$

for $t < a$, and by unity for $t \geq a$. Note that for $t \ll a$, this term is zero, whereas it approaches unity for $t = a$ at a rate determined by b . We have tested several combinations of a and b and found $a = 2 \text{ s}$ and $b = 0.5 \text{ s}$ in (6) to yield reasonable predictions; this approach is similar to that described in [15]. Here, 2 s is approximately one period of the long wave.

As the surface evolves in time, short waves have only a minimal effect on the evolution of the long wave, given their much smaller amplitude. The short wave spectrum, however, broadens from the truncated spectrum provided initially and exhibits some interactions among short waves. However, the dominant effect to be examined here is the variation in the local short wave spectrum with position on the long wave. For this purpose, localized short wave spectra will be introduced in Section III, so that the variation of these localized spectra with position on the long wave can be observed.

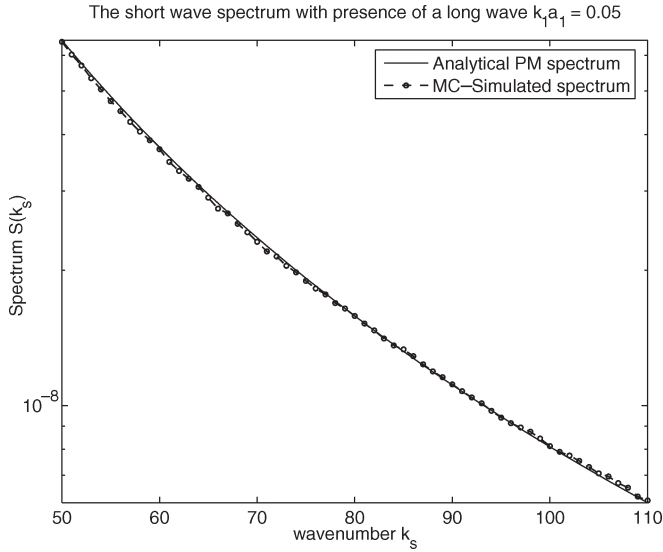


Fig. 1. Comparison of initial and final short wave spectra with $k_1 a_1 = 0.05$.

C. Other Information

The simulation was time stepped at $\Delta t = 0.001$ s for a duration of 5000 time steps (5 s) following the ramp-up period. Surface profiles were recorded every 0.1 s, providing 50 profiles per realization. The simulation was repeated using 1200 distinct short wave surface realizations, so that average spectra could be computed. Tests with larger numbers of realizations showed this choice to provide reasonable convergence for the results illustrated. Fig. 1 compares the initial input spectrum and final ensemble averaged spectrum of short waves in the presence of a long wave with $k_1 a_1 = 0.05$. The result shows that the short wave spectrum remains relatively constant during its evolution. The data set produced by the simulation consists of surface profile information $\eta(x_q, t_i, M_j)$, where x_q and t_i refer to the discretized horizontal and time coordinates, and M_j provides an index to the set of realizations generated.

III. DETERMINATION OF THE NUMERICAL HMTF

The configuration of this simulation allows long-short wave hydrodynamic modulations to be examined in detail. For this purpose, the computational domain in x is divided into subregions, and local Fourier transforms [using a fast Fourier transform (FFT) algorithm] are utilized to compute the spatially localized short wave spectrum for each region. The specific procedure is as follows.

1. Begin a loop over time t_i ;
2. Begin a loop over realizations M_j ;
3. Filter out all long wave components by passing the $\eta(x_q, t_i, M_j)$ surface through a spatial rectangular high-pass filter with cutoff $k_s = 30$ rad/m: call the resulting short wave surface $\eta_s(x_q, t_i, M_j)$;
4. Divide the x range into 31 spatial subregions, each subregion has a half overlap to its preceding one; label these subregions by their central x -values X_n ;
5. Begin a loop over subregions X_n ;

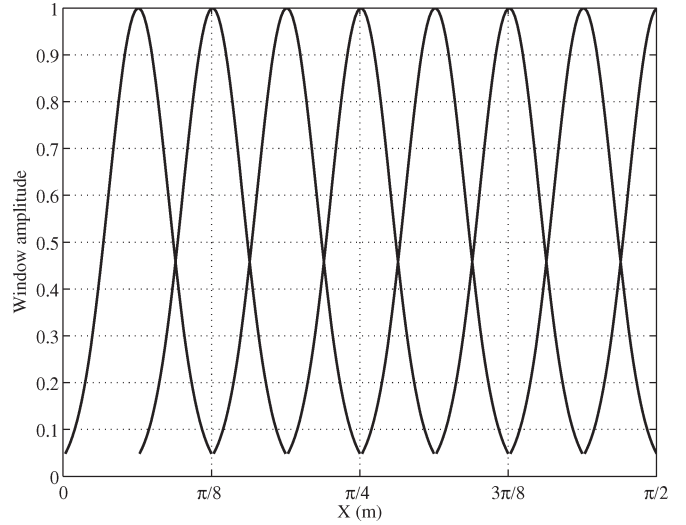


Fig. 2. Illustration of the first eight Gaussian windows used in defining spatial subregions.

6. Multiply $\eta_s(x_q, t_i, M_j)$ by a Gaussian window centered at X_n and perform an FFT zero padded to the length of the original profile on the result; denote FFT output as $\eta_{sn}(k_s, X_n, t_i, M_j)$;
7. Take $|\eta_{sn}(k_s, X_n, t_i, M_j)|^2$ to obtain the spectrum $S(k_s, X_n, t_i, M_j)$;
8. End loop over subregions;
9. End loop over realizations;
10. End loop over time.

In the above, the Gaussian window length is chosen as 64 points (~ 40 cm) with overlap 32 points, which results in 31 spatial subregions; a plot of the first several Gaussian windows is illustrated in Fig. 2. Parameters of the Gaussian function are chosen, so that the Gaussian is at e^{-1} at 18.1 points from the center of the filter. Tests varying these parameters within a reasonable range show only minor effects on the obtained MTF values.

The localized spectrum $S(k_s, X_n, t_i, M_j)$ can then be averaged over realizations to obtain the ensemble average localized spectrum $S_a(k_s, X_n, t_i)$, which describes the average evolution of the spectrum with time in a given subregion. This can be correlated to the approximate long wave phase versus time in that subregion, i.e.,

$$\Phi_l = k_1 X_n - \omega_1 t_i \tag{7}$$

where $\omega_1 = \sqrt{gk_1}$; it is also possible to determine the long wave phase numerically if desired. Because tests showed only minimal differences between these two methods, the former approach is utilized in the results shown. Finally, an additional average over time can be performed to obtain $\bar{S}(k_s, X_n)$, the ensemble and time average spectrum in a given subregion.

Fig. 3 illustrates the normalized quantity $S_a(k_s, X_n, t_i) / \bar{S}(k_s, X_n)$ for subregions 1, 5, 10, and 15 (relative initial long wave phases of $\pi/16, 5\pi/16, 10\pi/16$, and $15\pi/16$ rad, respectively) and for k_s values ranging from 50 to 100 rad/m, with $k_1 a_1 = 0.10$. The influence of the long wave

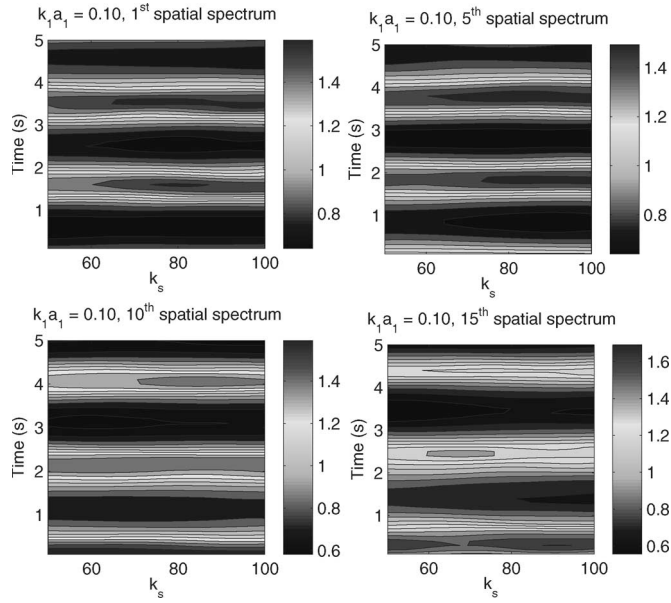


Fig. 3. Normalized-localized spectrum of $k_1 a_1 = 0.10$.

is clearly visible in these plots through the periodic variation in the normalized-localized spectra obtained; the period of the oscillation observed is consistent with that of the long wave. Although some variations from simple oscillations are obtained, the basic spectrum modulations are clearly correlated to the long wave phase in a given subregion.

Given this behavior, we define the numerical modulation $\mathfrak{R}(k_s, X_n, t_i)$ as follows:

$$\mathfrak{R}(k_s, X_n, t_i) = \frac{S_a(k_s, X_n, t_i) - \bar{S}(k_s, X_n)}{\bar{S}(k_s, X_n)}. \quad (8)$$

Note the spectrum in the denominator could be further averaged over subregions, but again, this modification does not yield significant variations in the obtained MTF values.

Fig. 4 plots an example value of \mathfrak{R} versus time ($k_s = 70$ rad/m in the tenth subregion). The oscillation of the spectrum is obvious, although an additional slow amplitude decay in time is observed that is not directly related to the long wave phase. We performed several tests of this slow decay and found it to be a much slower periodic function, evolving at a time rate involving the group velocity of the short wave spectrum. Although such effects do play a role in the evolution of the surface, and could likely be captured by a full simulation of the wave action equations, they are not of interest in studying first-order MTF effects, and therefore, a procedure for removing these slow time variations in extracting a numerical MTF value was developed.

Specifically, the following functional form was used to describe the short wave spectrum at a specified wavenumber and subregion:

$$\begin{aligned} \mathfrak{R}(k_s, X_n, t_i) \approx & b_{c0}(k_s, X_n) + b_{c1}(k_s, X_n) \sin(c_g(k_s) t_i) \\ & + b_1(k_s, X_n) \sin(k_1 X_n - \omega_1 t_i + \Phi_{01}(k_s, X_n)) \\ & + b_2(k_s, X_n) \sin(2k_1 X_n - 2\omega_1 t_i + \Phi_{02}(k_s, X_n)) \end{aligned} \quad (9)$$

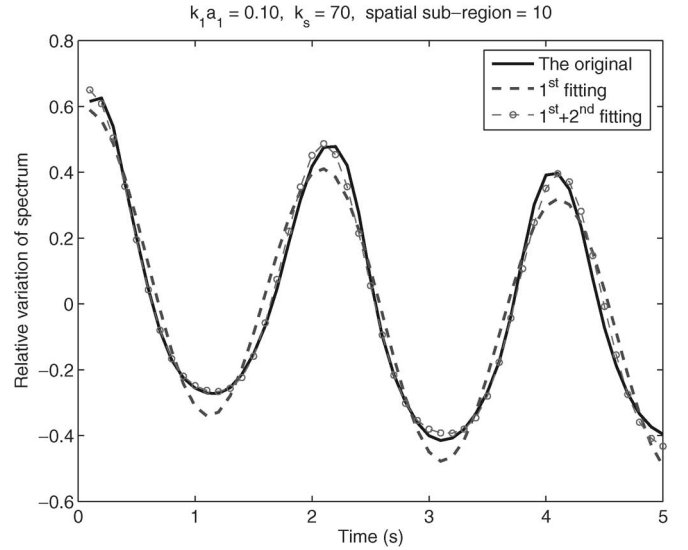


Fig. 4. Envelope of the total numerical HMTF versus time with $k_1 a_1 = 0.10$.

where c_g denotes the group velocity of the short wave at wavenumber k_s . In (9), the real-valued coefficients b_1 and Φ_{01} describe the amplitude and phase of a “first-order” numerical MTF, whereas the coefficients b_2 and Φ_{02} are included to allow some description of “second-order” effects. The coefficients b_{c0} and b_{c1} model an additive correction to account for the slow time evolution described previously. Other forms could be proposed as well, but the above definition appears to provide a reasonable means for extracting the portion of the spectrum modulation due to the long wave influence in the data set utilized. Unknown coefficients were determined using a least squares fitting procedure to the \mathfrak{R} data set; results were then averaged over subregions to obtain a final numerical value of the MTF, i.e., $\bar{b}_1(k_s)$. An alternative procedure involving a simultaneous fit to the data in all subregions was also considered; again, the results were practically identical to those using the procedure described and are therefore not discussed further.

IV. NUMERICAL HMTF RESULTS

A. One Long Wave

According to the wave action HMTF theory, the first-order coefficient $\bar{b}_1(k_s)$ should be directly proportional to $k_1 a_1$, and it is shown in [7] that the second-order coefficients should be proportional to $(k_1 a_1)^2$. Therefore, the results illustrated will be normalized by these quantities.

Fig. 5 plots normalized first- and second-order HMTF values ($\bar{b}_1(k_s)/(k_1 a_1)$ and $\bar{b}_2(k_s)/(k_1 a_1)^2$) obtained using $k_1 a_1 = 0.05$ and $k_1 a_1 = 0.10$. Results in the upper plot show the numerical \bar{b}_1 values to be approximately 4 in both long wave cases, with a difference from the value 4 on the order of 1% that depends weakly on k_s . The second-order coefficient is in the range 7–8.5 and shows a small decreasing trend as the long wave amplitude is increased.

HMTF phases averaged over subregions ($\bar{\Phi}_{01}$ and $\bar{\Phi}_{02}$) are plotted in Fig. 6. First-order phase results in the upper plot show values near 0° , with a very weak dependence on k_s and a slight trend (to -2°) versus the long wave amplitude. Second-order

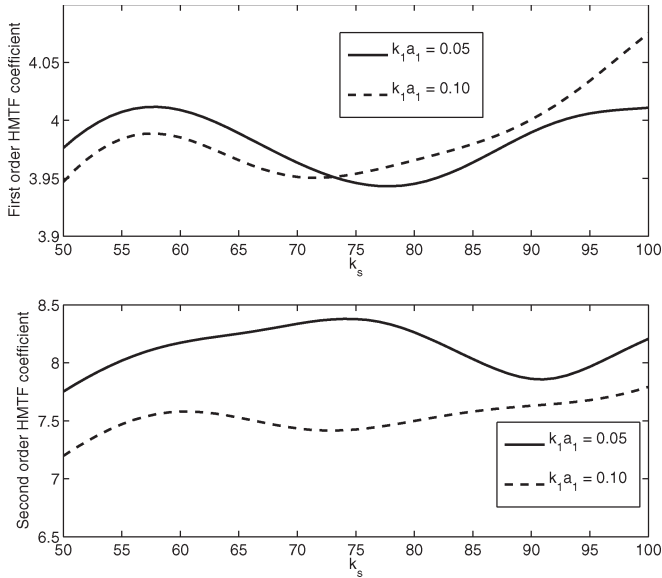


Fig. 5. Numerically obtained normalized HMTF amplitudes.

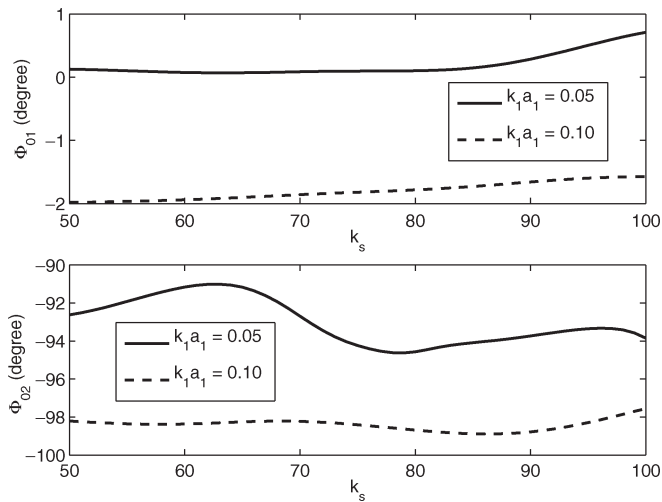


Fig. 6. Numerically obtained HMTF phase.

phases are near -90° , although the first-order values obtained are in the range -92 to -94° for the smaller long wave case and near -98° for the larger long wave case.

Although several potential sources of small errors exist in the values obtained, overall, the numerical results indicate that the first-order HMTF amplitude and phase are reasonably approximated as $4(k_1 a_1)$ and 0° in the data obtained, whereas the second-order coefficient (\bar{b}_2) is reasonably (but less reasonably than the first-order coefficient) approximated as $7.5(k_1 a_1)^2$ with a phase of -90° . Although more detailed analyses could be conducted to increase confidence in the prediction of any small deviations from these values, this basic information is sufficient for comparison with the first-order wave action theory, as will be performed in Section VI.

B. Two Long Waves

Additional numerical simulations were performed for initial conditions with two deterministic long waves, using $(k_1, a_1) =$

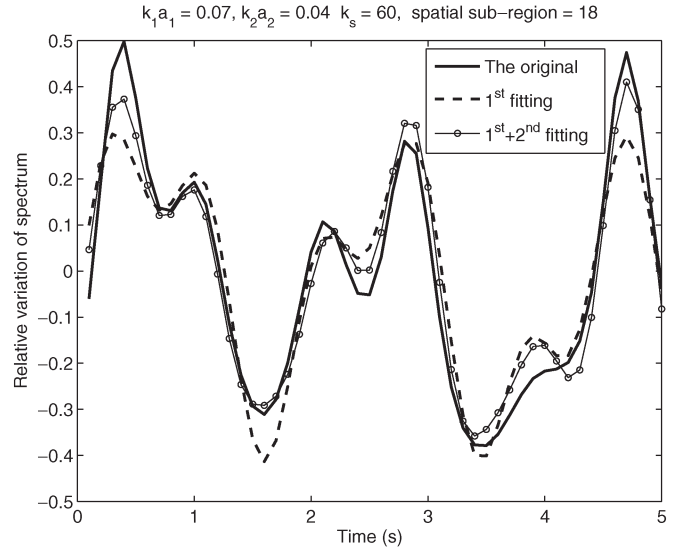


Fig. 7. Fitting of HMTF versus k_s with $k_1 a_1 = 0.07$ and $k_2 a_2 = 0.04$.

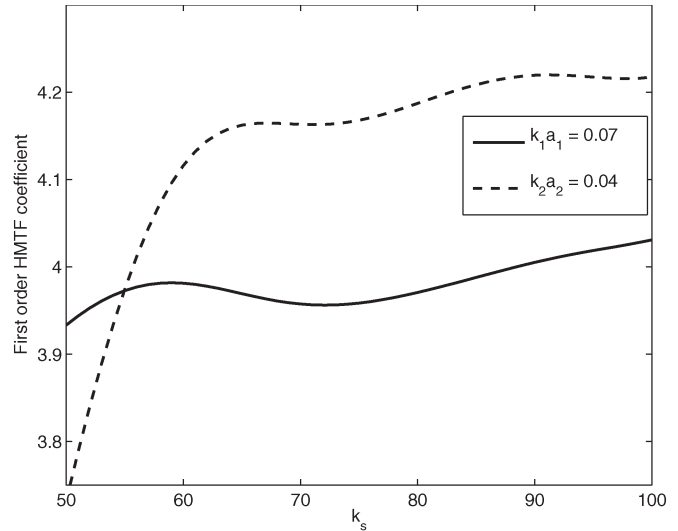


Fig. 8. Numerically obtained normalized HMTF amplitudes with $k_1 a_1 = 0.07$ and $k_2 a_2 = 0.04$.

$(1, 0.07)$ and $(k_2 = 5, a_2 = 0.008)$. Fig. 7 plots an example \mathfrak{R} , for $k_s = 60$ rad/m and in subregion 18, and shows that more complicated trends versus time are observed due to the presence of multiple long waves. The wave action theory at first order predicts that these trends should be due to a simple summation of the first-order effects from each long wave. Accordingly, the fitting function (9) was modified to include separate first- and second-order coefficients for the two long waves. Plots of the fit curves in Fig. 7 show that the fit accuracy is somewhat improved when second-order terms are included.

The two obtained normalized first-order MTF values averaged over spatial subregions are plotted in Fig. 8 and again are found to be near 4. However, the observed deviations from 4 are larger than those observed in the single long wave case, particularly for the k_2 wave. Again, detailed numerical studies could be conducted to assess these small deviations, but the basic conclusion from this analysis is that the linear summation

of first-order contributions from each long wave in computing combined modulation effects appears reasonable.

V. NUMERICAL STUDY OF THE SHORT WAVE DISPERSION RELATION

Modeling the effect of long waves on the dispersion relation of short waves is implicit in any wave action theory analysis of the HMTE. When short waves propagate over a slowly varying long wave or current, the short wave radian frequency ω is expected to undergo a Doppler shift [16], [17], i.e.,

$$\omega = \omega_s + \mathbf{k}_s \cdot \mathbf{U} \tag{10}$$

where ω_s is the short wave frequency in the absence of Doppler shift effects and \mathbf{U} is the underlying medium horizontal velocity with respect to the observer. Here, the dot product describes the relationship between the direction of the orbital velocity and the short wave propagation direction.

To study this Doppler shift, a new data set $\eta(x_q, t_i, M_j)$ was generated using $k_1 = 0.0625$ rad/m (wavelength and computational domain size 32π m). The long wave wavelength was extended in this case due to a desire to perform an additional temporal Fourier analysis of the short wave spectrum within a given subregion; use of longer long wave wavelengths results in an increased amount of time during which the long wave phase remains relatively constant in a given spatial subregion, so that the temporal Fourier analysis is more reasonable.

A time step of 0.002 s was used in the hydrodynamic simulations, with a total time duration of 20.48 s. The surface profile was discretized into 4096 points, and surface profile information was recorded every 0.04 s, so that 512 temporal samples are available during the time evolution. This time resolution is sufficient to capture the short wave temporal frequencies of interest. The short wave spectral range utilized in the simulations was $k_s \in [5, 15]$ rad/m. Other simulation parameters are similar to those described previously.

Analysis of the data set is similar to that used previously, with the exception that only 15 spatial subregions were used. In addition, the complete time history of FFT outputs of the surface within each spatial subregion was stored as the quantity $a(k_s, X_n, t_i, M_j)$; these are complex-valued Fourier coefficients versus time in each subregion. The 512-point time history of these Fourier coefficients was then divided into 15 overlapping time intervals labeled T_m through the use of Gaussian windows in time. An FFT of these localized time histories was then performed; the amplitude squared of this FFT output is then denoted as $\Omega(k_s, X_n, \omega_s, T_m, M_j)$ and includes the time history (on a long time scale T_m) of the radian frequency (ω_s) spectrum for the surface spectrum at wavenumber k_s in spatial subregion X_n . As in the previous analysis, this function can be ensemble averaged to eliminate the M_j dependence.

Fig. 9 illustrates ensemble averaged ω_s spectra versus time subregion T_m for the case $k_1 a_1 = 0.02$, $k_s = 10$ rad/m, and in several spatial subregions. The results appear consistent with a modulation in the short wave dispersion relation due to currents produced by the long wave orbital velocity. However, the observed ω_s spectra have nonzero width in frequency

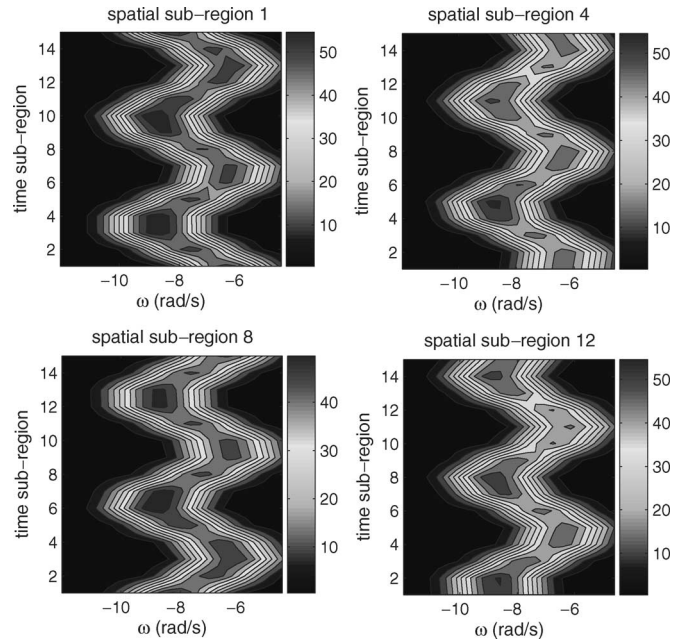


Fig. 9. Trajectories of ω_s with $k_1 = 1/16$ and $k_1 a_1 = 0.02$.

and show variations in amplitude that are more complex than (10) alone.

Using the ensemble averaged data set $\bar{\Omega}(k_s, X_n, \omega_s, T_m)$, we identify the value of ω_s that maximizes $\bar{\Omega}(k_s, X_n, \omega_s, T_m)$ for all other parameters fixed as $P(k_s, X_n, T_m)$. A least squares fit to the obtained $P(k_s, X_n, T_m)$ values is then performed using

$$P(k_s, X_n, T_m) = a_0(k_s, X_n) + c_0(k_s, X_n) \sin(k_1 X_n - \omega_1 T_m) \tag{11}$$

where a_0 should be approximately ω_s from (10), and c_0 represents the amplitude of the modulation due to long waves. Results for the a_0 and c_0 coefficients are then averaged over spatial subregions (X_n) to obtain $\bar{a}_0(k_s)$ and $\bar{c}_0(k_s)$.

Assuming that the current in the dispersion relation can be represented by the first-order horizontal component of the long wave orbital velocity, the predicted value of ω can be written as

$$\omega \approx \omega_s + k_s \omega_1 a_1 \sin(k_1 x - \omega_1 t) \tag{12}$$

with $\omega_s = \sqrt{gk_s}$. Fig. 10 plots the obtained coefficients normalized by their expected values (i.e., $\bar{a}_0(k_s)/\omega_s$ and $\bar{c}_0(k_s)/(k_s \omega_1 a_1)$); values near unity would indicate that the approximation of (12) is accurate. Results show the \bar{a}_0 term indeed to be well predicted by the theory, although the numerical results are slightly larger (by a factor less than 1%) than the prediction. The first-order modulation, however, is significantly less (around 0.88) than the predicted unity value, indicating that (12) may neglect some important effects. Numerically obtained coefficients show a slight increasing trend versus k_s in both cases.

Further dispersion studies were performed in an attempt to determine the source of the reduced numerical modulation compared with the first-order theory. Results show the offset between predictions to be near independent of $k_1 a_1$, so that the error is clearly at first order. To simplify the problem,

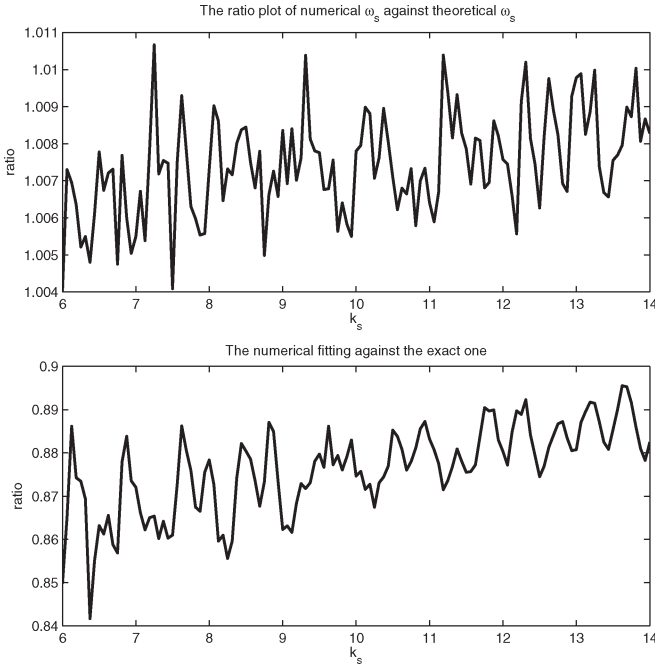


Fig. 10. Normalized dispersion relation coefficients $\bar{a}_0(k_s)/\omega_s$ (upper) and $\bar{c}_0(k_s)/(k_s\omega_1 a_1)$ (lower) with $k_1 = 1/16$ and $k_1 a_1 = 0.02$.

simulations were also performed using a deterministic single-frequency short wave packet, localized spatially on the long wave in the initial conditions; results again showed a similar offset in obtained frequency modulations. Consideration of the analytical theory suggests that corrections to the ω_s term may be relevant, involving either modulations of the wavenumber or local acceleration effects [7] involved in the definition of ω_s . Further investigation of these differences will be performed in future studies. Overall, the results show the standard first-order prediction of the local frequency to have reasonable, but not complete, accuracy.

VI. WAVE ACTION THEORY

The theory of wave action was developed for analysis of the evolution of a weakly nonlinear short wave “packet” as it propagates in an inhomogeneous background medium. The short wave packet consists of a narrowband set of waves centered around a carrier wavelength. In many water wave applications, the inhomogeneities encountered are current fields that vary slowly in space and/or time compared with the corresponding scales of the wave packet of interest. The concept of the conservation of wave action is based fundamentally on a separation of scales in both space and time, with packet properties described in terms of short scale wavenumber k_s and angular frequency ω_s parameters, whereas the slower variations are described in terms of x and t for space and time scales, respectively. The theory has been utilized to describe many phenomena of oceanographic interest, including the modulation of short waves by long waves relevant in this paper. Here, we follow the first-order solution of the wave action equation [4], [5], [7] developed to capture long–short wave modulation effects. Although a numerical solution of the wave action equation (as in [18]) for the configurations of this paper could be pursued, such

numerical solutions are far less frequently utilized in practice than the first-order solution and are therefore not considered further.

We also note that small differences in the form of the first-order HMTF are observed in the literature, for example, between [4] and [7]. These differences are partially explained by the inclusion of “heaving” effects not only due to the vertical component of the long wave orbital velocity in [7] but also due to the neglect of a group velocity term in the zeroth-order Lagrangian in [7]. Although other authors [4], [5] do not include the former, these other authors are uniformly in agreement that the latter is necessary. We choose to follow the formulation of [5] in what follows.

The wave action quantity N here is defined as [17]

$$N(k_s, x, t) = \frac{S(k_s, x, t)}{\omega_s} \quad (13)$$

where k_s is the local short wave wavenumber, $S(k_s, x, t)$ is the local short wave spectrum, and $\omega_s = \sqrt{gk_s}$ is the short wave radian frequency. For the purposes of this analysis, the wave action is modeled only for the short wave portion of the spectrum, and the dependencies on x and t result due to long wave effects that occur on the larger spatial and time scales. The analysis assumes that k and x are independent variables, although both depend on time.

Following [4], [5], [7], and [17], an equation describing the conservation of wave action can be written as

$$\frac{dN}{dt} = Q \quad (14)$$

where the differential operator d is the material derivative and operates along the characteristic or “ray” paths, whereas the term Q represents any sources or sinks of wave action. These include potential wind forcing, viscous damping, resonant nonlinear wave–wave interactions, or wave breaking [7] effects. Again, in practice, these terms are described primarily using empirical relations. The simulations performed include none of these sources or sinks with the exception of wave–wave interactions. However, because no strong resonant interactions are expected in the simulations, the term Q is set to zero in the remaining analyses.

For long–short wave modulation studies, it is convenient to rewrite (14) in phase space to

$$\frac{\partial N}{\partial t} + \dot{x} \frac{\partial N}{\partial x} + \dot{k}_s \frac{\partial N}{\partial k_s} = 0 \quad (15)$$

where the dot denotes the derivative with respect to time. The ray equations that describe the evolution of the canonical variables x and k_s are

$$\dot{x} = \frac{\partial \omega}{\partial k_s} = c_g + U \quad (16)$$

$$\dot{k}_s = -\frac{\partial \omega}{\partial x} = -k_s \frac{\partial U}{\partial x} \quad (17)$$

where $c_g = 1/2\sqrt{g/k_s}$ is the short wave group velocity for the wavenumber considered, and U is the horizontal component of the long wave orbital velocity.

A. Determination of HMTF

Following [4] and [5], a perturbative solution to first order is sought. A description of the long wave orbital velocity consistent with this goal is

$$U = \omega_1 a_1 \sin(\Phi) \tag{18}$$

where $\Phi = k_1 x - \omega_1 t$ denotes the long wave phase.

Because it is modulations of the spectrum, not of wave action, that are of interest in the studies of this paper, the substitutions

$$\frac{\partial N}{\partial t} = \frac{1}{\omega_s} \frac{\partial S}{\partial t} \tag{19}$$

$$\frac{\partial N}{\partial x} = \frac{1}{\omega_s} \frac{\partial S}{\partial x} \tag{20}$$

$$\frac{\partial N}{\partial k_s} = \frac{1}{\omega_s} \frac{\partial S}{\partial k_s} - \frac{c_g}{\omega_s^2} S \tag{21}$$

$$= -\frac{S}{\omega_s k_s} [m + \gamma_s] \tag{22}$$

are utilized to recast (15) in terms of the short wave spectrum alone; (22) holds when it is assumed that the spectrum assumes the form $\bar{S} \propto \bar{k}_s^{-m}$ as given in (5). The quantity $\gamma_s(k_s)$ is given by $c_g(k_s)/c_p(k_s)$, where c_g and c_p are the group and phase velocities of the short wave considered, respectively; for purely gravity waves, $\gamma_s = 0.5$. Note that it is assumed in (19) that the value of ω_s used in the denominator of the wave action definition is independent of time; this will be considered further below.

Substituting the above equations into (15) and combining with (16) and (17) yields

$$\frac{\partial S}{\partial t} + c_g \frac{\partial S}{\partial x} = -U \frac{\partial S}{\partial x} - [m + \gamma_s] S \frac{\partial U}{\partial x}. \tag{23}$$

A perturbation solution is now performed, in which the orbital velocity U is assumed to be the small parameter. Writing

$$S = S^{(0)} + S^{(1)} + \dots \tag{24}$$

yields at zeroth order

$$\frac{\partial S^{(0)}}{\partial t} + c_g \frac{\partial S^{(0)}}{\partial x} = 0. \tag{25}$$

The above can be transformed into an ordinary differential equation by introducing the variables

$$\alpha = x - c_g t \tag{26}$$

$$\beta = x + c_g t \tag{27}$$

to obtain

$$\frac{\partial S^{(0)}}{\partial \beta} = 0. \tag{28}$$

The solution to this equation is that $S^{(0)}$ is constant in β while remaining arbitrary in α . However, if an initial condition of the zeroth-order solution is chosen that is independent of x at time zero (as is appropriate for the studies described here), the result is that $S^{(0)}$ is independent of x and t .

Continuing to first order, the relevant equation is

$$\frac{\partial S^{(1)}}{\partial t} + c_g \frac{\partial S^{(1)}}{\partial x} = -[m + \gamma_s] S^{(0)} \frac{\partial U}{\partial x} \tag{29}$$

with the linear term in U vanishing due to the constant nature of $S^{(0)}$. Substituting the specified form for U , and again making use of the variable transformation described previously, allows this equation to be solved. The result is

$$S^{(1)} = k_1 a_1 \sin(\Phi) \frac{[m + \gamma_s]}{1 - \frac{c_g}{c_1}} S^{(0)} \tag{30}$$

where $c_1 = \sqrt{g/k_1}$ is the long wave phase velocity.

Because $S^{(1)}$ above is directly proportional to $\sin \Phi$, the predicted HMTF can now be determined in terms of

$$\frac{S^{(1)}}{S^{(0)} \sin(\Phi)} \tag{31}$$

with the magnitude and phase of this quantity defined as R_1 and Φ_1 , respectively. Substituting (30) in (31) and solving yields

$$R_1 = (k_1 a_1) \frac{[m + \gamma_s]}{1 - \frac{c_g}{c_1}} \tag{32}$$

$$\Phi_1 = 0. \tag{33}$$

This HMTF prediction is identical to that in [5].

Although only a single long wave was considered in this derivation, the linear nature of the first-order solution ensures that the combined effect of two long waves to first order is simply the sum of their individual contributions.

B. Comparison With Numerical Simulations

For the numerical simulations performed, the spectrum utilized had a k_s^{-3} dependence, yielding $m = 3$ for use in (32). In addition, the value of γ_s is 0.5 for gravity waves, so that the predicted value of R_1 can be simplified to

$$(k_1 a_1) \frac{3.5}{1 - \frac{1}{2} \sqrt{\frac{k_1}{k_s}}}. \tag{34}$$

Factoring out $k_1 a_1$ as in Fig. 5, the remaining coefficient ranges from a value of 3.766 at $k_s = 50$ rad/m to 3.684 at $k_s = 100$ rad/m with $k_1 = 1$ rad/m, as compared with the observed values near 4 from the numerical simulations (Figs. 5 and 8). The predicted phase of 0° is well matched by the numerical simulations.

Although further studies of the differences between the numerical and analytical models could be performed, overall, the results indicate that the first-order HMTF derived from wave action theory yields reasonable (within 10%) predictions of short wave modulations by longer sea waves. It is noted that this difference remains consistent even as the long wave amplitude is decreased; this fact motivates continued studies to improve upon the wave action theory formulation applied here.

One possible correction involves inclusion of time variations in ω_s in computing the time derivative of the wave action, so that

$$\frac{\partial N}{\partial t} = \frac{1}{\omega_s} \frac{\partial S}{\partial t} - \frac{c_g}{\omega_s^2} S \frac{\partial k_s}{\partial t} \quad (35)$$

as opposed to (19). The result of this modification is a change in the value 3.5 in (34) to 4; the final predicted HMTF values now exceed 4 by 5%–8%, whereas the original values were less than 4 by similar percentages. Therefore, no clear improvement results from this change.

A second possible correction involves the inclusion of local acceleration effects as described in [7]. In this case, the gravitational acceleration is modified along the long wave by the vertical long wave acceleration; this change in the local gravitational acceleration is modeled by introducing an additional $-\partial\tilde{\omega}_s/\partial x$ term on the right-hand side of (17). The local frequency is given by

$$\tilde{\omega}_s = \sqrt{\tilde{g}k_s} \quad (36)$$

within which only \tilde{g} is considered a function of x . The method for determining the local gravitational acceleration \tilde{g} is described in [7]. Following this process results in a change in (34) to

$$(k_1 a_1) \frac{3.5 \left(1 + \frac{1}{2} \sqrt{\frac{k_1}{k_s}}\right)}{1 - \frac{1}{2} \sqrt{\frac{k_1}{k_s}}} \quad (37)$$

which varies from 4.033 at $k_s = 50$ rad/m to 3.87 at $k_s = 100$ rad/m when normalized. Although these values are closer to those obtained numerically, the inclusion of local acceleration effects in fact increases the error in the short wave dispersion relation fits described in Section V. For this reason, the modeling of local acceleration effects used here cannot be considered completely validated.

Although further extensions of the wave action theory to include other effects or second-order contributions for comparison with the second order numerically obtained results are possible, the first-order theory described here is most commonly used in practice and is the most relevant in applications. Further examinations of improvements to the wave action theory are left for future work.

VII. CONCLUDING REMARKS

A numerical study of the modulation of short sea waves by longer waves was performed to provide an assessment of the first-order HMTF commonly used in remote sensing of the sea. The use of numerical simulations allowed examination of the

theory in a controlled environment without need for empirical models of effects such as wind forcing and wave breaking. Results show the first-order HMTF to provide a reasonable prediction of the short wave modulations observed in the numerical simulations. Numerical results also show the basic applicability of the standard Doppler-shifted dispersion relation in the cases considered. However, in both of these areas, differences on the order of 10% from the commonly used analytical theories were encountered, indicating that revisions to the standard first-order forms may be possible to yield improved predictions.

Future work will include further analysis of the basic wave action theory formulation and its first- and second-order HMTF predictions, as well as more detailed numerical simulations over a wider range of short and long wave environments. The numerical procedures presented here should be applicable to such studies with only minor modifications.

ACKNOWLEDGMENT

The authors would like to thank G. Baker (Ohio State Department of Mathematics), D. Lyzenga (University of Michigan), and W.-Y. Choi (New Jersey Institute of Technology) for helpful discussions.

REFERENCES

- [1] M. S. Longuet-Higgins and R. W. Stewart, "Changes in the form of short gravity waves on long waves and tidal currents," *J. Fluid Mech.*, vol. 8, pp. 565–583, 1960.
- [2] —, "The changes in amplitude of short gravity waves on steady non-uniform currents," *J. Fluid Mech.*, vol. 10, pp. 529–549, 1961.
- [3] T. Hara and W. J. Plant, "Hydrodynamic modulation of short wind-wave spectra by long waves and its measurement using microwave backscatter," *J. Geophys. Res.*, vol. 99, no. C5, pp. 9767–9784, May 1994.
- [4] W. Alpers and K. Hasselmann, "The two-frequency microwave technique for measuring ocean-wave spectra from an airplane or satellite," *Boundary-Layer Meteorol.*, vol. 13, no. 1–4, pp. 215–230, Jan. 1978.
- [5] B. A. Hughes, "The effect of internal waves on surface wind waves: Theoretical analysis," *J. Geophys. Res.*, vol. 83, no. C1, pp. 455–465, Jan. 1978.
- [6] E. A. Caponi, D. R. Crawford, and H. C. Yuen, "Modulation of radar backscatter from the ocean by a variable surface current," *J. Geophys. Res.*, vol. 93, no. C10, pp. 12 249–12 263, Oct. 1988.
- [7] T. Elfouhaily, D. R. Thompson, D. Vandemark, and B. Chapron, "Higher-order hydrodynamic modulation: Theory and applications for ocean waves," *Proc. R. Soc. Lond. A, Math Phys. Sci.*, vol. 457, no. 2015, pp. 2585–2608, Nov. 2001.
- [8] J. T. Johnson and Y. Y. Cai, "A theoretical study of sea surface up/down wind brightness temperature differences," *IEEE Trans. Geosci. Remote Sens.*, vol. 40, no. 1, pp. 66–78, Jan. 2002.
- [9] B. J. West, K. Brueckner, R. S. Janda, D. Milder, and R. Milton, "A numerical method for sea surface hydrodynamics," *J. Geophys. Res.*, vol. 92, no. C11, pp. 11 803–11 824, 1987.
- [10] D. G. Dommermuth and D. K. P. Yue, "A high-order spectral method for the study of nonlinear gravity waves," *J. Fluid Mech.*, vol. 184, pp. 267–288, 1987.
- [11] M. Tanaka, "A method of studying nonlinear random field of surface gravity waves by direct numerical simulation," *Fluid Dyn. Res.*, vol. 28, no. 1, pp. 41–60, 2001.
- [12] K. M. Berger, G. R. Baker, and J. T. Johnson, "A comparison of nonlinear water wave models," *Int. J. Comput. Fluid Dyn.*, vol. 17, no. 3, pp. 219–224, May 2003.
- [13] J. T. Johnson, J. V. Toporkov, and G. S. Brown, "A numerical study of backscattering from time-evolving sea surfaces: Comparison of hydrodynamic models," *IEEE Trans. Geosci. Remote Sens.*, vol. 39, no. 11, pp. 2411–2420, Nov. 2001.
- [14] A. R. Hayslip, J. T. Johnson, and G. R. Baker, "Further numerical studies of backscattering from time evolving non-linear sea surfaces," *IEEE Trans. Geosci. Remote Sens.*, vol. 41, no. 10, pp. 2287–2293, 2003.

- [15] D. G. Dommermuth, "The initialization of nonlinear waves using an adjustment scheme," *Wave Motion*, vol. 32, no. 4, pp. 307–317, 2000.
- [16] G. B. Whitham, "A note on group velocity," *J. Fluid Mech.*, vol. 9, pp. 347–352, 1960.
- [17] F. P. Bretherton and C. J. R. Garrett, "Wavetrains in inhomogeneous moving media," *Proc. R. Soc. Lond. A, Math. Phys. Sci.*, vol. 302, no. 1471, pp. 529–554, 1968.
- [18] P. A. Hwang and O. H. Shemdin, "Modulation of short waves by surface currents: A numerical solution," *J. Geophys. Res.*, vol. 95, no. C9, pp. 16 311–16 318, 1990.

Guangdong Pan received the B.E. degree in geosciences from the Chengdu University of Technology, Chengdu, China, in 1992, the M.S. degree in cartography and remote sensing from the Chinese Academy of Sciences, Beijing, China, in 1998, and the M.S. degree in electrical engineering from the University of Nebraska, Lincoln, in 2003. He is currently working toward the Ph.D. degree at The Ohio State University, Columbus.

From 1998 to 2001, he was with the Chinese Academy of Sciences as a Research Associate for the first two years and later as a Research Assistant Professor. His research interests include scattering and propagation in random media and computational electromagnetics.

Joel T. Johnson (S'89–M'91–SM'03) received the Bachelor's degree in electrical engineering from the Georgia Institute of Technology, Atlanta, in 1991, and the S.M. and Ph.D. degrees from the Massachusetts Institute of Technology, Cambridge, in 1993 and 1996, respectively.

He is currently a Professor with the Department of Electrical and Computer Engineering and ElectroScience Laboratory, The Ohio State University, Columbus. His research interests are in the areas of microwave remote sensing, propagation, and electromagnetic wave theory.

Dr. Johnson is a member of the Commissions B and F of the International Union of Radio Science (URSI) and a member of Tau Beta Pi, Eta Kappa Nu, and Phi Kappa Phi. He received the 1993 Best Paper Award from the IEEE Geoscience and Remote Sensing Society, was named an Office of Naval Research Young Investigator, National Science Foundation Career awardee, and PECASE award recipient in 1997, and was recognized by the U.S. National Committee of URSI as a Booker Fellow in 2002.